

# Nanoscale current transport in epitaxial SrTiO<sub>3</sub> on *n*<sup>+</sup>-Si investigated with conductive atomic force microscopy

D. M. Schaadt and E. T. Yu<sup>a)</sup>

*Department of Electrical and Computer Engineering, University of California at San Diego, La Jolla, California 92093*

V. Vaithyanathan and D. G. Schlom

*Department of Materials Science and Engineering, Pennsylvania State University, University Park, Pennsylvania 16802*

(Received 18 January 2004; accepted 9 April 2004; published 18 August 2004)

We have used conductive atomic force microscopy to image the nanoscale current distribution in SrTiO<sub>3</sub> grown epitaxially on *n*<sup>+</sup>-Si by molecular beam epitaxy. Topographic and current images were obtained simultaneously in contact mode with a bias voltage applied to the sample. Topographic images show a flat surface with a roughness of about 0.5 nm. Current images show small areas with local current flow on the order of pA for voltages larger than ~2 V in forward bias and larger than ~4 V in reverse bias. Histograms of the magnitude of the electrical current show a relatively narrow log-normal distribution, suggesting a common current mechanism with a Gaussian distribution in a parameter on which the current depends exponentially. Analysis of current images and histograms over a range of bias voltages suggests thermionic emission as the dominant current mechanism, rather than conduction associated with localized defects such as pin-holes, threading dislocations or grain boundaries. The analysis yields a barrier height of ~0.5–0.6 eV with and a relative dielectric constant of 5–15, which is in reasonable agreement with previous reports using a dead layer model. © 2004 American Vacuum Society. [DOI: 10.1116/1.1768529]

## I. INTRODUCTION

SrTiO<sub>3</sub> has been suggested by some<sup>1,2</sup> as a candidate for application as a high- $\kappa$  dielectric gate oxide replacement for SiO<sub>2</sub> in future metal-oxide-semiconductor field-effect-transistors due to its high bulk dielectric constant ( $\epsilon > 180$ )<sup>3</sup> and the possibility of epitaxial growth on Si by pulsed laser deposition,<sup>4,5</sup> electron beam deposition,<sup>6,7</sup> or molecular-beam epitaxy (MBE).<sup>8</sup> Recent studies of the electrical characteristics of SrTiO<sub>3</sub> grown on Si have shown relatively low leakage currents compared to other high- $\kappa$  dielectrics of similar equivalent oxide thickness.<sup>9</sup> However, these measurements were performed with standard, large area electrodes and the detailed nature of the current mechanisms remains unknown. Scaling of MOSFET gate sizes to the sub-100 nm regime necessitates a detailed investigation of the nanoscale current distribution and determination of the relevant physical mechanisms of current flow. We have used conductive atomic force microscopy (CAFM) to image the nanoscale current distribution in SrTiO<sub>3</sub> grown epitaxially on *n*<sup>+</sup>-Si by MBE. Investigating the current images and using a statistical analysis of histograms of the current magnitude in the current images, we find that the current is dominated by thermionic emission and not related to localized defects such as pin-holes or threading dislocations. A detailed description and analysis of the current distribution is presented.

## II. EXPERIMENTAL PROCEDURE

The epitaxial layer structure used in these studies was grown by MBE on a *n*<sup>+</sup>-Si substrate with a dopant concen-

tration of  $5 \times 10^{18} \text{ cm}^{-3}$ . The silicon substrate was exposed to ozone for 20 min to remove the surface organics, prior to loading in the MBE chamber. The base pressure in the chamber was  $\sim 1-2 \times 10^{-9}$  Torr. In vacuum, the wafer was heated to 930 °C to desorb the native SiO<sub>2</sub> layer on the surface, which resulted in a clean 2× starting silicon template. The substrate was then cooled to  $\sim 700$  °C, followed by a deposition of 1/2 monolayer (ML) of Sr. The deposited Sr reacts with silicon and forms a submonolayer silicide template. This silicide template is more stable to oxygen exposure and prevents the formation of amorphous SiO<sub>2</sub> at the interface;<sup>10</sup> thus promoting the epitaxial growth of oxides on silicon. Following this, the wafer was cooled to 100 °C for the deposition of 3 ML of SrO ( $P_{\text{O}_2} \sim 4 \times 10^{-8}$  Torr). 3 ML SrO were deposited even at low temperatures is crystalline, but relaxed because of the large mismatch (−5.2%) with silicon. Two monolayers of amorphous TiO<sub>2</sub> were deposited on top of the crystalline SrO stack at <100 °C in an oxygen ambient of  $3 \times 10^{-7}$  Torr. In vacuum, a recrystallization anneal was performed by heating the wafer to 550 °C to enable the formation of epitaxial SrTiO<sub>3</sub> by a topotactic reaction. This topotactic reaction involves the diffusion of amorphous TiO<sub>2</sub> layers through the crystalline SrO stack resulting in the formation of crystalline epitaxial SrTiO<sub>3</sub>.<sup>11</sup> Further growth of epitaxial SrTiO<sub>3</sub> on this two unit cell template was achieved by repeated low temperature deposition of few unit cells (~5) of amorphous SrTiO<sub>3</sub> (co-deposition of Sr and Ti in an oxygen partial pressure of  $2-3 \times 10^{-7}$  Torr), followed by vacuum recrystallization anneal at 550 °C. A schematic drawing of the sample structure is shown in Fig. 1.

Topographic and current images were recorded simulta-

<sup>a)</sup>Electronic mail: ety@ece.ucsd.edu

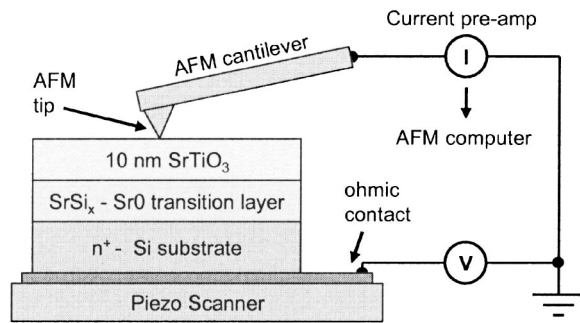


FIG. 1. Schematic diagram of the sample structure and the measurement configuration for conductive atomic force microscopy.

neously in contact mode in a Digital Instruments Multimode atomic force microscope modified for CAFM measurements,<sup>12</sup> as shown in Fig. 1. Measurements were performed under ambient conditions with relative humidity of 55%–65%. The current images were obtained by applying a bias voltage to the sample and measuring the current through a conductive diamond-coated tip  $p^+$ -doped with boron. All current images were obtained with a pre-amp amplification factor of  $10^{-9}$  A/V.

### III. RESULTS AND DISCUSSION

#### A. Topographic and current images

Figure 2 shows topographic and current images obtained simultaneously for sample bias voltages  $V_S$  of 4.5 and  $-1$  V. The topographic images reveal the surface to be quite flat, with a rms roughness of about 0.5 nm, measured over an area

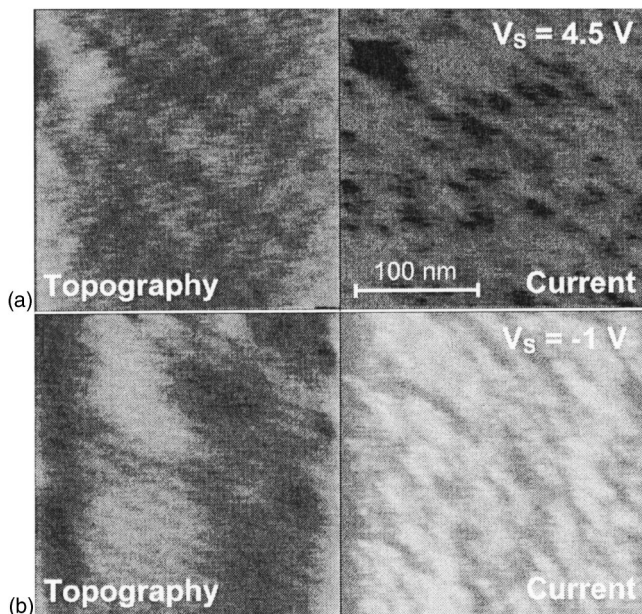


FIG. 2. Topographic (left) and current (right) images obtained simultaneously in contact-mode with a sample bias  $V_S$  of (a) 4.5 V and (b)  $-1$  V. The gray scale ranges are 2 nm for the topographic and 0.5 nA for the current images. The current images show local irregularly shaped conductive areas which are uncorrelated to the topography. Conductive areas are observed in both reverse and forward bias.

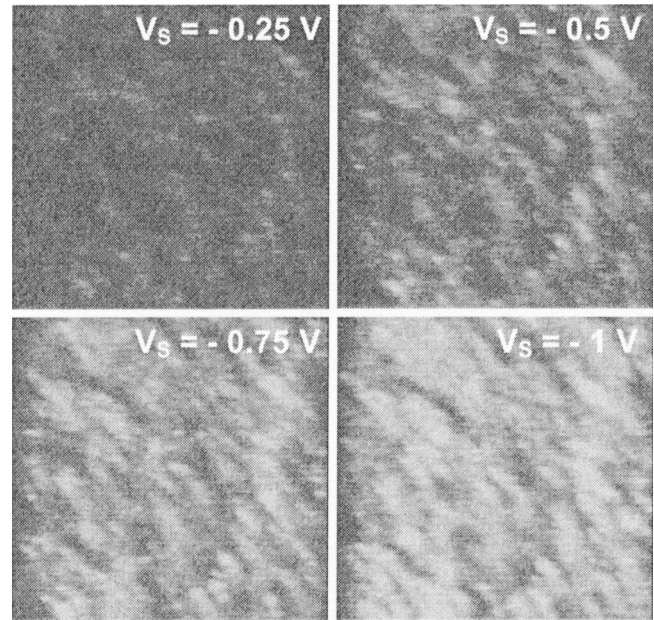


FIG. 3. Series of current images obtained with increasing forward bias, scanning over the same area. As the bias is increased, the conductive areas grow in size and additional conductive areas appear. The gray scale range of the images is 0.5 nA.

of  $4 \mu\text{m}^2$ . The current images show highly localized, irregularly shaped conductive areas which are uncorrelated to the topography. Highly conductive areas are observed in both reverse and forward bias. Imaging of the current flow process does not induce topographic changes on the sample surface, as has been observed to occur in atomic force microscopy (AFM) nanolithography experiments and CAFM measurements on GaN.<sup>12</sup> A slight decrease in current is observed, however, after repeated scanning.

#### B. Current-voltage characteristics

To determine the dependence of the current distribution on the applied bias voltages, a series of images with varying forward bias ranging from  $-0.25$  to  $-1$  V was obtained on the same area, as shown in Fig. 3. As the bias voltage magnitude increases the conductive areas become more pronounced and grow in size, and additional conductive areas appear. This indicates that the conductive areas are not associated with individual localized defects such as threading dislocations or pin-holes but rather are due to intrinsic film properties such as variations in barrier height or film thickness.

To obtain quantitative data on the current magnitude as a function of applied bias voltage, a series of current images was obtained for sample bias ranging from 6.5 V in reverse bias to  $-6.5$  V in forward bias, as shown in Fig. 4. To avoid any effects of surface modification induced by the scanned probe tip, the probe tip was moved to a new area before the bias was changed. Conductive features are clearly visible for reverse bias voltages larger than  $\sim 4$  V and forward bias voltages beyond  $\sim -2$  V.

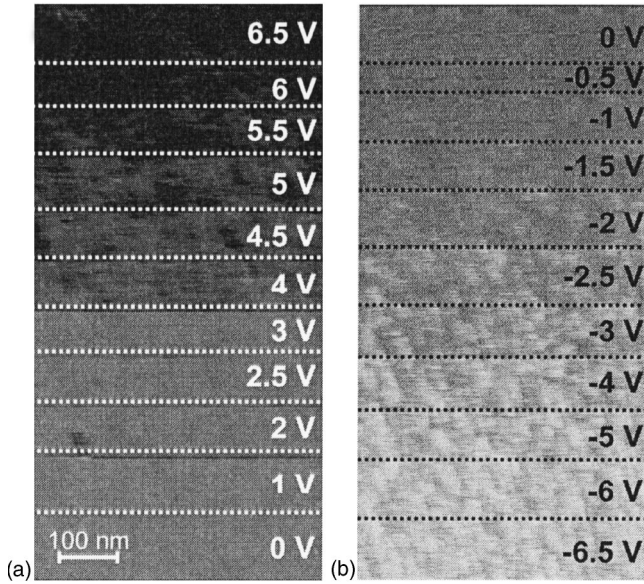


FIG. 4. Series of current images as a function of increasing forward and reverse bias. The gray scale range is 1 nA. As the magnitude of the bias increases, the conductive areas become more pronounced.

Figure 5 shows histograms of the current magnitude for select sample biases, derived from the images in Fig. 4. Each histogram was obtained using a constant area (434 pixels×34 pixels) and a bin size of 2.5 pA. The histograms show a log-normal distribution in current magnitude, i.e.,

$$n(I) = \frac{A_I}{\sqrt{2\pi\sigma_I I}} e^{-[\ln(I) - \ln(I_0)]^2 / 2\sigma_I^2}, \quad (1)$$

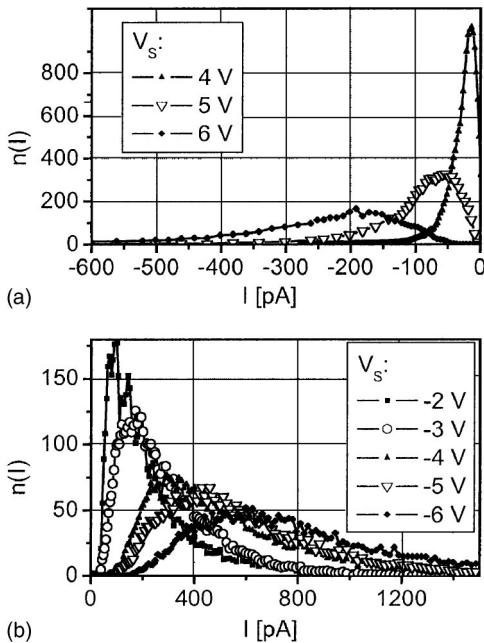


FIG. 5. Histograms of the electrical current magnitude for selected bias voltages. The current distributions are log-normal with single peaks that shift to larger current values with increasing bias voltage magnitude.

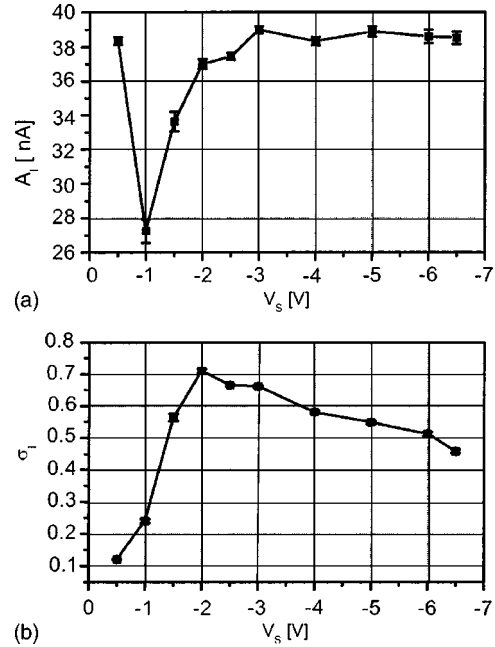


FIG. 6. Current distribution function normalization  $A_I$  and variance  $\sigma_I$  as functions of bias voltage.

where  $I_0$  is the histogram peak position,  $A_I$  is a normalization factor, and  $\sigma_I$  is the variance. The log-normal distribution in current magnitude indicates that the observed conductivity arises from a single current mechanism with exponential dependence of the current on a parameter exhibiting a Gaussian distribution. Fitting current-magnitude histograms for all applied forward bias voltages to Eq. (1) yields average values  $A_I \sim 36.7 \pm 4$  nA and  $\sigma_I \sim 0.5 \pm 0.2$ , as shown in Figs. 6(a) and 6(b), respectively. The values are relatively independent of voltage for voltages larger than 1.5 V and are, as expected, smaller by a factor of about two to four for smaller applied bias voltages, for which the current is comparable to or smaller than the measurement resolution.

A plot of the peak current  $I_0$  as a function of voltage  $V_S$  is shown in Fig. 7. A large series resistance of about 5 GΩ is evident at high current levels, correction for which yields the series-resistance-adjusted values shown in the figure (open symbols).  $\ln I_0$  as a function of the square root of the electric field within the oxide,  $E = V/t$ , is plotted in Fig. 7(b) as measured (solid symbols) and after correction for series-resistance effects (open symbols); an oxide thickness  $t = 10$  nm is assumed. A linear region is clearly visible at low bias voltage (low electric field), suggesting that the dominant current mechanism is thermionic emission, for which

$$I(V) = AA^* T^2 e^{-\phi_B/kT} e^{1/kT \sqrt{qV/(4\pi\epsilon_0\kappa t)}}, \quad (2)$$

where  $A \pi r_{\text{tip}}^2$  is the tip-sample contact area,  $A^*$  is the Richardson constant,  $\phi_B$  the electron barrier height at the diamond-oxide interface,  $k$  the Boltzmann constant,  $T$  the temperature,  $q$  the electron charge,  $\epsilon_0$  the vacuum permittivity,  $\kappa$  the oxide dielectric constant, and  $t$  the oxide thickness. This is in agreement with a previous study<sup>13</sup> in which thermionic emission is suggested as the dominant mechanism for

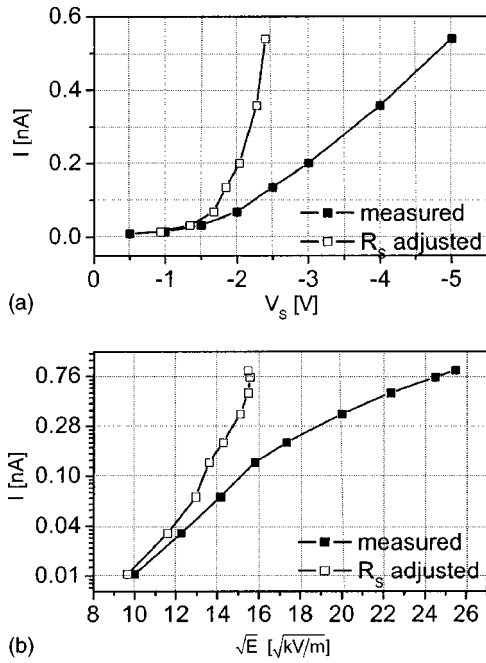


FIG. 7. (a) Current-voltage characteristics as measured (solid symbols) and adjusted for series resistance effects (open symbols). (b)  $\ln I_0$  vs the square root of the electric field as measured (solid symbols) and adjusted for series resistance effects (open symbols).

thin SrTiO<sub>3</sub> films and bulk-limited thermionic emission<sup>14</sup> for thicker SrTiO<sub>3</sub> films where the mean-free path of electrons is smaller than the film thickness. For larger applied biases, the slope decreases as a result of series resistance or distortion of the tip-sample contact as often observed for large applied bias in CAFM.

Fitting the current  $I_0$  at low fields using the thermionic emission model of Eq. (2) yields a barrier height  $\phi_B = 0.52 \text{ eV} \pm 0.5 \text{ meV}$  assuming a Richardson constant of  $600 \text{ A/cm}^2$  (Ref. 15) and a tip radius of curvature  $r_{\text{tip}} = 10 \text{ nm}$ , or  $0.60 \text{ eV} \pm 0.5 \text{ meV}$  for  $r_{\text{tip}} = 50 \text{ nm}$ , and a dielectric constant  $\kappa = 16.27 \pm 0.06$ . Fitting to the series resistance adjusted curve yields similar values:  $\phi_B = 0.59 - 0.68 \text{ eV} \pm 0.5 \text{ meV}$  and  $\varepsilon = 5.1 \pm 0.01$ .

The barrier height is in good agreement with that derived from a numerically calculated band diagram, shown in Fig. 8(a), obtained using a self-consistent one-dimensional (1D)-Poisson/Schrödinger solver<sup>16</sup> for a  $p^+$ -doped diamond tip with an electron affinity of approximately 0 V (Refs. 17, 18) placed on top of SrTiO<sub>3</sub> grown on Si. The calculation was performed assuming a conduction band offset of 0 V between SrTiO<sub>3</sub> and Si<sup>19</sup> and unpinned surface Fermi levels due to the unknown electronic nature of the surface. Thermionic emission is only possible as a current mechanism if electron states exist in the diamond tip near the interface between diamond and SrTiO<sub>3</sub> at energies near the conduction band edge of SrTiO<sub>3</sub>. A solution of Schrödinger's equation for the above band diagram near the interface of diamond and SrTiO<sub>3</sub> using the 1D-Poisson solver indicates that the electron wave functions of the conduction band states in SrTiO<sub>3</sub> extend several angstroms into the diamond tip. This

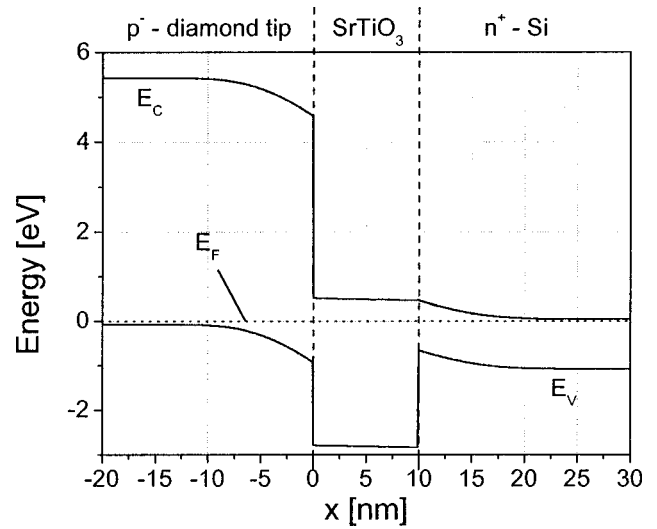


FIG. 8. Numerically calculated band diagram of the  $p^-$ -doped diamond coated probe tip on SrTiO<sub>3</sub> on  $n^+$ -Si. An acceptor concentration of  $5 \times 10^{18} \text{ cm}^{-3}$  and an electron affinity of 0 V were assumed for the diamond tip, while the conduction band offset between SrTiO<sub>3</sub> and the Si substrate was set to 0 eV.

suggests that states should exist in the diamond near the conduction band edge of SrTiO<sub>3</sub> and therefore enable thermionic emission through these states. The extracted dielectric constant is much lower than the bulk value of  $\sim 300$ , but is in reasonable agreement with previous reports<sup>3,20</sup> for films thicker than 23 nm if those values are extrapolated to 10 nm using the reported  $1/t$  dependence. The low dielectric constant is explained in these reports as a consequence of dead interface layers exhibiting a lower dielectric constant than bulk SrTiO<sub>3</sub>.

The log-normal distribution in current magnitude observed experimentally implies that the current depends exponentially on a parameter exhibiting a normal distribution. Assuming thermionic emission as the current mechanism, possible parameters can be the barrier height or the product of the dielectric constant and the thickness. The variance  $\sigma_{\phi_B}$  of the barrier height and  $\sigma_{\kappa t}$  of the product of  $\kappa t$  can be related to the variance  $\sigma_I$  in current by

$$\sigma_{\phi_B} = \sigma_I kT, \quad (3a)$$

$$\sigma_{\kappa t} \approx \sigma_I \frac{2(\kappa t)_0^{3/2} kT}{q} \sqrt{\frac{4\pi\varepsilon_0}{qV}}. \quad (3b)$$

As mentioned earlier, the observed variance  $\sigma_I$  is approximately constant with respect to voltage. We therefore conclude that the observed variations are due to a distribution in barrier height with  $\sigma_{\phi_B} \sim 13 - 18 \text{ meV}$ .

#### IV. CONCLUSIONS

We have used conductive atomic force microscopy (CAFM) to image the nanoscale current distribution in SrTiO<sub>3</sub> grown epitaxially on  $n^+$ -Si by MBE. Topographic and current images were obtained simultaneously in contact mode with a bias voltage applied to the sample. Topographic

images show a flat surface with a roughness of about 0.5 nm. For voltage magnitudes larger than  $\sim 2$  V in forward and  $\sim 4$  V in reverse bias, the current images reveal small areas with local current flow on the order of pA. These features are irregularly shaped with an approximate radius of about 10–50 nm and are not correlated with any topographic features. As the bias is increased, the features grow in size and current magnitude and additional conductive areas appear, indicating that the current is not associated with localized defects such as pin-holes, threading dislocations, grain boundaries, or other extended defects. Histograms of electrical current magnitude show a log-normal distribution with a variance of  $\sim 0.5$  over a large bias range, suggesting that the current conduction arises due to a current mechanism which depends exponentially on a parameter exhibiting a Gaussian distribution. Analysis of current histograms shows that thermionic emission appears to be the dominant current mechanism with a barrier height of  $\sim 0.5$ – $0.6$  eV exhibiting variations on the order of 13–18 meV. The relative dielectric constant deduced from our measurements ranges between 5 and 16; values in this range are in reasonable agreement with previous reports invoking the existence of a dead interface layer exhibiting a lower dielectric constant than bulk SrTiO<sub>3</sub>.

#### ACKNOWLEDGMENTS

D.M.S. acknowledges useful discussions with Blake S. Simpkins. Part of this work was supported by NSF (Award No. DMR 0072912).

- <sup>1</sup>K. Eisenbeiser, J. M. Finder, Z. Yu, J. Ramdani, J. A. Curless, J. A. Hallmark, R. Droopad, W. J. Ooms, L. Salem, S. Bradshaw, and C. D. Overgaard, *Appl. Phys. Lett.* **76**, 1324 (2000).
- <sup>2</sup>R. Droopad, Z. Yu, J. Ramdani, L. Hilt, J. Curless, C. Overgaard, J. L. Edwards, Jr., J. Finder, K. Eisenbeiser, and W. Ooms, *Mater. Sci. Eng., B* **87**, 292 (2001).
- <sup>3</sup>K. Abe and S. Komatsu, *Jpn. J. Appl. Phys., Part 2* **32**, L1157 (1993).
- <sup>4</sup>F. Sánchez, R. Aguiar, V. Trtik, C. Guerrero, C. Ferrater, and M. Varela, *J. Mater. Res.* **13**, 1422 (1998).
- <sup>5</sup>O. Nakagawara, M. Kobayashi, Y. Yoshino, Y. Katayama, H. Tabata, and T. Kawai, *J. Appl. Phys.* **78**, 7226 (1995).
- <sup>6</sup>H. Mori and H. Ishiwara, *Jpn. J. Appl. Phys., Part 2* **30**, L1415 (1991).
- <sup>7</sup>B. K. Moon and H. Ishiwara, *Jpn. J. Appl. Phys., Part 1* **33**, 1472 (1994).
- <sup>8</sup>R. A. McKee, F. J. Walker, and M. Chisholm, *Phys. Rev. Lett.* **81**, 3014 (1998).
- <sup>9</sup>S. Jeon, F. J. Walker, C. A. Billman, R. A. McKee, and H. Hwang, *IEEE Electron Device Lett.* **24**, 218 (2003).
- <sup>10</sup>Y. Liang, S. Gan, and M. Engelhard, *Appl. Phys. Lett.* **79**, 3591 (2001).
- <sup>11</sup>V. Vaithyanathan, J. Lettieri, J. Haeni, L. Edge, J. Schubert, and D. G. Schlom (unpublished).
- <sup>12</sup>E. J. Miller, D. M. Schaadt, E. T. Yu, C. Poblentz, C. Elsass, and J. S. Speck, *J. Appl. Phys.* **91**, 9821 (2002).
- <sup>13</sup>S. Zafar, R. E. Jones, B. Jiang, B. White, V. Kaushik, and S. Gillespie, *Appl. Phys. Lett.* **73**, 3533 (1998).
- <sup>14</sup>J. G. Simmons, *Phys. Rev. Lett.* **15**, 967 (1965).
- <sup>15</sup>H. P. R. Frederikse, W. R. Hosler, and W. R. Thurber, *Phys. Rev.* **143**, 648 (1966).
- <sup>16</sup>G. L. Snider, *Computer Program 1D Poisson/Schrödinger: A Band Diagram Calculator*, University of Notre Dame, 1995.
- <sup>17</sup>K. Liu, B. Zhang, M. Wan, J. H. Chu, C. Johnston, and S. Roth, *Appl. Phys. Lett.* **70**, 2891 (1997).
- <sup>18</sup>K. W. Wong, S. T. Lee, Z. Lin, Y. W. Lam, and R. W. M. Kwok, *Jpn. J. Appl. Phys., Part 1* **38**, 791 (1999).
- <sup>19</sup>S. A. Chambers, Y. Liang, Z. Yu, R. Droopad, and J. Ramdani, *J. Vac. Sci. Technol. A* **19**, 934 (2001).
- <sup>20</sup>C. Zhou and D. M. Newns, *J. Appl. Phys.* **82**, 3081 (1997).